Journal of Physics D:
Applied Physics

PAPER • **OPEN ACCESS**

Atmospheric EAD grid thruster performance: a theoretical–experimental approach on geometry and pressure effects

To cite this article: D Usuelli *et al* 2026 *J. Phys. D: Appl. Phys.* **59** 015203

Journal of Physics D: Applied Physics

OPEN ACCESS

RECEIVED
10 September 2025

REVISED
5 November 2025

ACCEPTED FOR PUBLICATION
27 November 2025

PUBLISHED
24 December 2025

PAPER

Atmospheric EAD grid thruster performance: a theoretical–experimental approach on geometry and pressure effects

D Usuelli*, A Favalli, S Trovato, R Terenzi and M Belan

Department of Aerospace Science and Technology (DAER), Politecnico di Milano, Via La Masa 34, 20156 Milano, Italy
* Author to whom any correspondence should be addressed.

E-mail: davide.usuelli@polimi.it

Keywords: EAD performances, pressure, corona discharge, grid geometry, gap

Abstract

In this work, a wire-to-grid electroaerodynamic thruster is experimentally investigated in a low-pressure environment. The study explores the influence of electrode gap d and ambient pressure p on thrust density T/A, thrust-to-power ratio T/P, and corona current i_c. A dedicated test rig is designed to operate within a low-pressure chamber, which is equipped with diagnostics for thrust and electrical measurements. Experimental results are compared with a revised physical model. The findings validate the theoretical framework and reveal that thruster performance is highly sensitive to both pressure and electrode spacing. Overall performance degrades with decreasing pressure, while optimal values of T/A and T/P require a trade-off in the selection of gap. Measurements of ignition and breakdown voltages further define the operational envelope, showing an expansion with increasing pressure.

1. Introduction

In recent years, the aerospace community has increasingly focused on environmentally friendly propulsion solutions for air vehicles, ranging from small general aviation aircraft and unmanned drones to large commercial planes and stratospheric platforms such as air balloons and airships. Electric propulsion systems [1, 2] and hydrogen-based technologies [3] have emerged as leading candidates for reducing carbon footprints. In this frame, electro-aerodynamic (EAD) thrusters are gaining attention as a promising alternative to traditional propeller-driven systems. Originally developed for space applications [4–6], EAD thrusters have recently attracted interest for atmospheric use due to their simple design, absence of moving parts, and low noise emissions. Unlike ion thruster used in space, atmospheric versions do not require an onboard propellant tank as they utilize ambient air to generate thrust. This feature enhances both the operational lifetime and the mission flexibility of the system. Notable prototypes demonstrate the feasibility of this propulsion concept [7, 8], though the technology remains in an early stage of development with significant room for improvement. Current EAD thruster operates under corona discharge regime, characterized by a self-sustained current that arises when a sufficiently high voltage (HV) difference is applied across two electrodes: an emitter and a collector. Ionization occurs at the emitter, ions are generated and accelerated in the gap region, known as drift region. As these travel, they collide with neutral air molecules, transferring momentum and creating an ionic wind that generates thrust. The ions eventually neutralize upon reaching the collector. There are two types of corona discharge: positive and negative. The positive regime is typically used in EAD thrusters, where positive ions travel through the drift region, while negative ions remain localized near the emitter [9, 10]. A key requirement for air ionization is the presence of a strong asymmetric electric field, typically achieved by employing electrodes with different radii of curvature. Thin metallic wires with a diameter below 200μm are commonly employed as emitters, however other solutions are possible such as blades [11–13] or pins [14–16]. Collectors are often shaped like airfoils [7, 17], droplets [8] or cylinders [18]. A basic thruster unit, composed of one emitter and one collectors, can be stacked in parallel [19, 20] or

arranged sequentially to create a multi-staged thruster [21, 22]. Various optimization studies in the literature explore configurations and geometric parameters such as the gap distance d, emitter spacing s_e, collector spacing s_c, and their relative arrangement [20, 21, 23, 24]. EAD thruster performances are affected by an electrostatic phenomenon known as shielding [25, 26]. Although shielding can negatively impact ionization if it occurs near the emitters, it can be advantageous when occurring near the collectors. By inducing field asymmetry, shielding allows for compact and lightweight collector designs with reduced aerodynamic drag. This concept was explored in [27] using grid collectors made of wires with similar diameters to the emitters, resulting in improved performance compared to traditional thruster configurations.

Various ionization sources for EAD thrusters have been investigated [28–31], but DC corona discharge remains the most effective option. Nowadays wind tunnel experiments have also been conducted to evaluate performance with an asymptotic flow [32–34]. While most tests to date have been performed in controlled laboratory environments, EAD thrusters are intended for real-world and also high-altitude applications [35, 36]. Therefore, recent studies have examined the influence of atmospheric variables such as pressure, temperature, and humidity on system performance [37–40]. Performance metrics for EAD thrusters typically include thrust density (T/A), an index of compactness, thrust-to-power ratio (T/P), an index of efficiency, power consumption (P_c) and current consumption (i_c), with A a reference frontal area. Alternatively, dimensionless coefficients have been proposed [23, 24] to allow for more consistent comparisons between different configurations.

The objective of this work is to experimentally evaluate a state-of-the-art EAD thruster featuring grid-based collectors under varying atmospheric pressure p and electrode gap distance d in a low pressure chamber. In parallel, a revision of existing theory is proposed to develop a comprehensive model that considers all parameters affecting performance. The key focus is to understand how performance varies as a function of p and d and to define the operational envelope between the ignition voltage V_{ign}, onset of corona discharge, and the breakdown voltage V_{br} that marks the transition to a different regime.

This paper is organized as follows: section 2 presents the theoretical model, section 3 describes the experimental setup, section 4 illustrates the design of experiment, section 5 discusses the results and compares them to the theoretical model, finally section 6 concludes the paper.

2. Theoretical model

This section presents a theoretical model developed to generate dimensionless performance coefficients and predict the thruster's behavior as a function of atmospheric pressure p and electrode gap d. The framework is developed following the footsteps of the work discussed in [23, 37, 39]. The fundamental principle of thrust generation in EAD devices involves the collisions between ions and neutral particles, characterized by the collision frequency $\nu_{\text{ions}\leftrightarrow\text{neutrals}}$ which depends on air density ρ. The thermodynamic state of air is fully determined by two independent intensive properties: pressure p and temperature Θ, such that $\rho = f(p, \Theta)$. In this experimental campaign, only pressure could be controlled within the low pressure chamber, while temperature always corresponded to ambient conditions. Although temperature was not actively controlled, it was continuously monitored throughout the test campaign, a mean value of $\Theta = 21.2 \pm 0.7\,^{\circ}\text{C}$ was registered. As a result, the theoretical framework assumes $\Theta = \text{const}$ and $\rho = f(p)$. The second key parameter, the electrode gap d, has been extensively studied in the literature [41, 42]. It is the primary geometrical parameter influencing thruster performance, with the electrode arrangement held fixed. Given that the electrical envelope of an EAD thruster, defined as the difference between breakdown voltage and ignition voltage, is expected to shrink as pressure decreases, the electrode gap d may be an important factor in determining the optimal operating point of the thruster at a given altitude.

The present analysis starts from the theoretical study [23] which led to the derivation of dimensionless performance coefficients which, in turn, facilitate better comparison between different thruster configurations. These coefficients are listed in table 1.

where ϵ_0 is the dielectric permittivity, μ is the ion mobility, V_a is the applied voltage, A is a frontal reference area. It is important to emphasize that in this derivation $V_a = V_c$ where V_c is the voltage across electrodes, assuming an ideal electric circuits. However, in a laboratory setting, $V_a > V_c$ because of the losses and of the possible use of a ballast resistor, and corona voltage V_c should be used when applying these coefficients. Upon analyzing the reference values, according to this derivation, thrust density T/A is

Table 1. Performance coefficients from [23].

Name	Reference value	Coefficient
Thrust density, $\frac{T}{A}$	$\epsilon_0 \frac{V_a^2}{d^2}$	C_{TA}
Thrust to power, $\frac{T}{P}$	$\frac{d}{\mu V_a}$	C_{TP}
Corona current, i_c	$\mu\epsilon_0 \frac{V_a^2}{d^3}$	C_C

expected to scale as $1/d^2$. In contrast, literature [18, 41, 42] suggests an inversely proportional dependence with respect to electrode gap. Moreover, the scaling law derived in [23] does not account for variations of environmental factors such as pressure and temperature. Additionally, all performance parameters are shown to scale with the applied voltage only, thus disregarding any dependence on the ignition voltage (which is in turn a function of pressure and gap), below which no corona discharge develops.

2.1. Performance coefficients

This section revises the derivation of the above performance coefficients, with a focus on defining the correct scaling with respect to ignition voltage V_{ign}, electrode gap d and pressure p.

As previously discussed, the characteristics of corona discharge depend on air density ρ. This dependence is manifested through the ion mobility μ which is governed by the balance between the electrostatic force imparted by an external electric field and the collisional drag arising from interactions with neutral background species. According to kinetics theory [43], ion mobility is defined as $\mu = q/(m\nu_m)$, where q is the charge of the species, m its mass and ν_m the momentum transfer collision frequency. The collision frequency is a linear function of density, such that $\nu_m \propto \rho$. Following Langevin kinetics theory [44], which is commonly applied in this context, ion mobility can be expressed as:

$$\frac{\mu(\Theta,p)}{\mu_0} = \frac{\Theta}{273.15\,\mathrm{K}} \frac{101.325\,\mathrm{kPa}}{p} = \frac{\kappa(\Theta)}{p} \tag{1}$$

where μ_0 is the ion mobility under standard condition, called reduced ion mobility. From this expression, it is clear that ion mobility is inversely proportional to pressure.

2.1.1. Corona current: C_C

Corona current arises from ions drift between electrodes. An EAD thruster operates under corona discharge regime, charges build up modifying the local electric field thus limiting the maximum amount of current, this behavior is described by Mott–Gurney law, a limiting case which sets the maximum possible current density in the drift region: $j_{MG} = (9/8)\mu\epsilon_0(V_c^2/d^3)$. This can be used as a scaling variable to define the dimensionless corona current coefficient C_C:

$$C_C = \frac{i_c}{j_{MG}A} = \frac{8}{9}\frac{i_c}{\mu_0\kappa\epsilon_0 A}\frac{d^3 p}{V_c \Delta V}. \tag{2}$$

The dependence on pressure is made explicit using (1). The applied voltage V_a^2 has been substituted by $V_c\Delta V$ where $\Delta V = V_c - V_{ign}$ to consider the threshold voltage required for the discharge to develop. This dependence of current on voltage has already been shown in several studies [18, 28].

2.1.2. Drift region EAD equations

The physics of the drift region can be described by the drift region equations:

$$\nabla \cdot \mathbf{E} = \frac{\rho_q}{\varepsilon_0} \tag{3a}$$

$$\nabla \cdot \mathbf{j} = \nabla \cdot \rho_q(\mu\mathbf{E} + \mathbf{u}) = 0 \tag{3b}$$

$$\rho(\mathbf{u}\cdot\nabla\mathbf{u}) = -\nabla p + \mu_f \nabla^2 \mathbf{u} + \rho_q \mathbf{E} \tag{3c}$$

where $\mathbf{E}$ is the electric field vector, ρ_q is the space charge density, $\mathbf{u}$ is the hydrodynamic bulk velocity while μ_f is the fluid dynamic viscosity. They represent first Maxwell law, current density continuity and Navier–Stokes respectively; in the latter the volumetric EAD Coulomb force is added as a source term.

System (3) is made dimensionless introducing scaling variables. The first Maxwell law is of particular interest as it defines the scaling values for space charge density. The nondimensionalization of the equations is carried out starting with the following relations:

- $\mathbf{x} = d\,\hat{\mathbf{x}}$, the spatial coordinate system is made dimensionless by the gap distance d;

- $\mathbf{E} = (V_c/d)\ \hat{\mathbf{E}}$, a reference electric field is defined by ratio of the applied voltage to the electrode gap;
- $\rho_q = \rho_0\ \hat{\rho_q}$, space charge density is scaled with a reference value ρ_0.
- $\mathbf{u} = u_0\ \hat{\mathbf{u}}$, the hydrodynamic bulk velocity is scaled with a reference value u_0.

Substituting these definitions in (3*a*) leads to the dimensionless form of Poisson equation:

$$\hat{\nabla} \cdot \hat{\mathbf{E}} = \frac{\rho_0 d^2}{V_c \epsilon_0} \hat{\rho}_q. \tag{4}$$

A reference value for the charge density can be defined in such a way that the multiplicative term has order 1:

$$\rho_0 = \epsilon_0 \frac{V_c}{d^2}. \tag{5}$$

This reference value does not show any dependence on pressure, due to the insufficient modeling of space charge density. This is an inherent limitation of a low dimensional model: in fact, considering that the thrust is the integral of the product $\rho_q E$ in space, under the assumption of a given reference electric field $E = V_c/d$, the only quantity that can affect thrust when pressure varies is ρ_q. In other words, the variation in thrust level with pressure for a fixed gap must be driven by the variation of charge density. Hence, a new reference value is suggested here for space charge density ρ_q:

$$\rho_0 = \epsilon_0 \frac{\Delta V}{d^2} \frac{pd}{\chi} \tag{6}$$

the *pd* product introduces the explicit dependence on pressure and also modifies the scaling law for the discharge gap. The parameter χ is introduced to keep the coefficient dimensionless. The *pd* product is also the independent variable in the well-known Paschen curves [43], which describe the breakdown and regime change processes in gas discharge, this curve always has a minimum called Stoletov point which is a constant for a given thruster geometry. For this reason χ is set to be $\chi = (pd)_{\text{Stoletov}}$. The introduction of ΔV considers the threshold voltage required for the discharge to develop. This formulation also introduces a different trend with respect to the gap, suggesting that in a low dimensional framework the charge density should be a linear function of the electric field, thus correcting also the discrepancy in thrust versus gap previously encountered in literature [23]. The goodness of this new modeling is discussed in section 5.

The steady state current continuity equation (equation (3*b*)), in dimensionless form, can be written as:

$$\nabla \cdot \rho_0\ \hat{\rho_q} \left(\underbrace{\mu \frac{V_c}{d}}_{u_{\text{drift}}}\ \hat{\mathbf{E}} + u_0\ \hat{\mathbf{u}} \right) = 0 \quad \rightarrow \quad \nabla \cdot \hat{\rho_q} \left(\hat{\mathbf{E}} + R_v\ \hat{\mathbf{u}} \right) = 0 \tag{7}$$

where a new dimensionless number appears: $R_v = (u_0/u_{\text{drift}})$ representing the ratio between the hydrodynamic velocity and a reference ion drift velocity $u_{\text{drift}} = \mu(V_c/d)$. Its effect, widely studied in [34], results in only a minor increase in current and can therefore be considered negligible for very low-velocity conditions, such as those encountered within a variable-pressure vessel, as in the present study. Finally, introducing the scaling variables in equation (3*c*) yields the classical dimensionless form of the Navier–Stokes equations, in which the Reynolds number based on the gap Re_d naturally emerges.

2.1.3. Thrust density: C_{TA}

The thrust force generated is defined as the integral of EAD force density over the thruster domain Ω.

$$T = \int_{\Omega} \rho_q E \mathrm{d}\Omega. \tag{8}$$

Substituting the previously defined scaling variables, thrust density coefficient C_{TA} can be derived as:

$$T/A = \epsilon_0 \frac{\Delta V}{d} \frac{p}{\chi} \frac{V_c}{d} d \underbrace{\int_{\hat{\Omega}} \hat{\rho_q} \hat{E} \mathrm{d}\hat{\Omega}}_{C_{TA}}. \tag{9}$$

Table 2. Analytical expressions and dependencies of dimensionless coefficients.

Coefficient	Expression	Proportionality wrt (V, p, d)
C_{TA}	$\frac{T\chi d}{A\epsilon_0 p V_c \Delta V}$	$\frac{d}{pV_c\Delta V}$
C_{TP}	$\frac{9T\chi\kappa\mu_0 V_c}{8Pp^2d^2}$	$\frac{V_c}{p^2d^2}$
C_C	$\frac{8i_c d^3 p}{9\mu_0\kappa\epsilon_0 A V_c \Delta V}$	$\frac{d^3p}{V_c\Delta V}$

2.1.4. Corona power: C_P

The power drained by the thruster is computed by its integral definition:

$$P = \int_\Omega \mathbf{j}\cdot\mathbf{E}\mathrm{d}\Omega. \tag{10}$$

The substitution with scaling variables leads to the definition of power coefficient C_P as:

$$P = \frac{9}{8}\frac{\kappa\mu_0}{p}\epsilon_0\frac{V_c\Delta V}{d^3}\frac{V_c}{d}\,dA\underbrace{\int_{\hat\Omega}\hat{\mathbf{j}}\cdot\hat{\mathbf{E}}\mathrm{d}\hat\Omega}_{C_P}. \tag{11}$$

2.1.5. Thrust to power: C_{TP}

Thrust-to-power coefficient is computed according to (9) and (11):

$$\frac{T}{P} = \frac{8}{9}\cdot\frac{p^2}{\kappa\mu_0\chi}\cdot\frac{d^2}{V_c}\cdot\underbrace{\frac{\int_{\hat\Omega}\hat\rho_q\hat E\mathrm{d}\hat\Omega}{\int_{\hat\Omega}\hat{\mathbf{j}}\cdot\hat{\mathbf{E}}\mathrm{d}\hat\Omega}}_{C_{TP}}. \tag{12}$$

The derived performance coefficients are listed in table 2, where in the third column the proportionality with respect to studied variables are highlighted, voltage levels are included since the operational envelope of the thruster depends on pressure level through V_{ign}.

3. Experimental setup

This section describes the experimental setup used throughout the test campaign, section 3.1 described the facility and the diagnostics installed, section 3.2 describes the geometry of the thruster, section 3.3 discusses the data elaboration techniques.

3.1. Test facility and diagnostics

The experimental campaign was conducted in a low pressure chamber as shown in figure 1. The facility features a modular cylindrical steel assembly consisting of three sections: the head, the central segment and the tail. Each segment is 750 mm in length with a nominal inner diameter of 500 mm. The connection between different sections is secured by dedicated flanges, the entire vessel is electrically grounded. The chamber is capable of maintaining pressures on the order of few pascals. The tail and central section has no access points while the head section features multiple access ports. A tempered glass window is installed on the top to monitor the nominal operation of the thruster. The desired pressure level is achieved using a single-stage rotary vane pump connected to a lateral port. Manual valves regulate air outflow and inflow from ambient air. A manometer with resolution 2000 Pa is installed to monitor chamber pressure.

Two access ports are allocated to electrical connections. An HV feedthrough delivers the supplied voltage from the power supply unit (PSU) to the thruster. Given that the EAD thruster operates at kilovolts voltage levels, the HV feedthrough is appropriately insulated to prevent electrical breakdown and arc formation. The PSU provides an output voltage range from 0 kV to 30 kV DC. A 60-pin feedthrough located at the bottom of the head section accommodates all low-voltage (LV) lines.

Thrust is measured using a single load cell; installation details are provided in section 3.2. The load cell features a full-scale range of 1.5 kg and a resolution of 0.1 g. Signal routing from the load cell is carried through the LV feedthrough. Additional LV wiring is used for grounding. All LV cables are enclosed within EMI shielding braid to minimize susceptibility to electromagnetic interference.

An electrical circuit is implemented to power the thruster and measure the relevant operational parameters. These include the corona voltage V_c, defined as the potential difference across the electrodes, and the corona current i_c, representing the current flowing from emitters to collectors. A ballast resistance

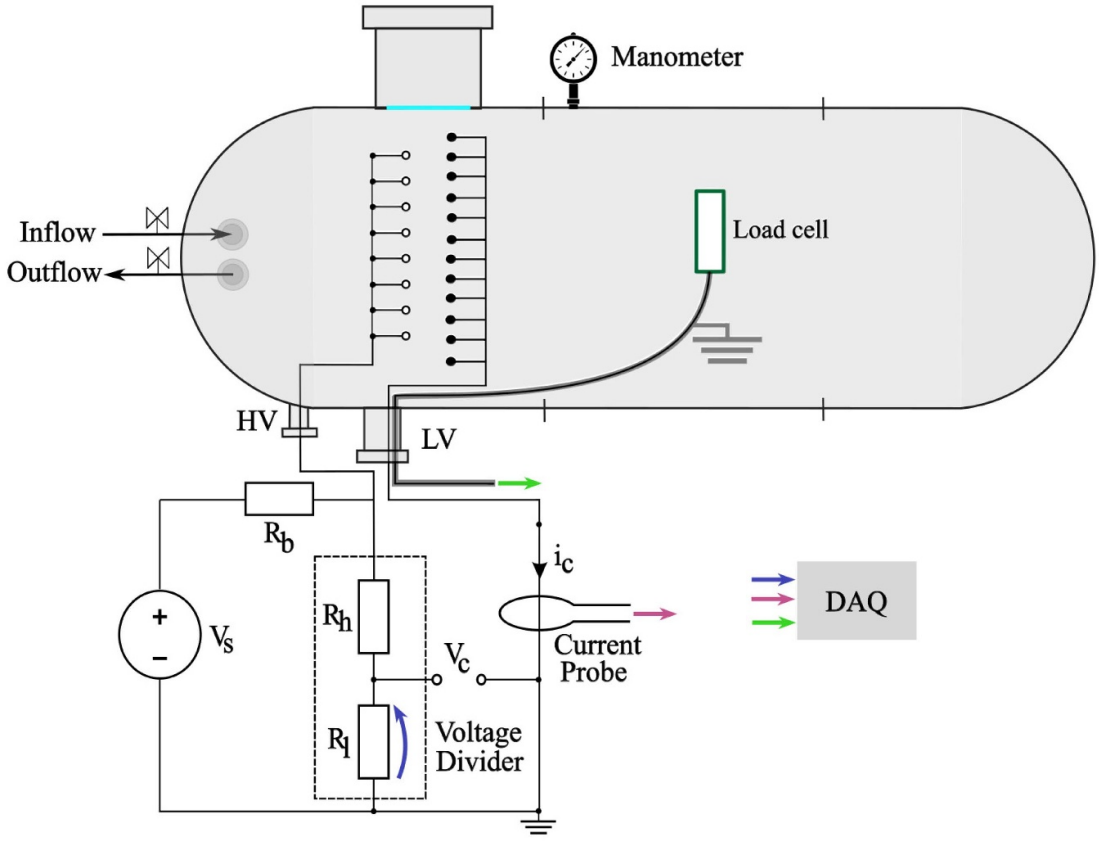

Figure 1. Schematic diagram of the test facility. Colored arrows indicate acquired signals.

$R_b = 4.4 \pm 0.0005\,M\Omega$ is connected in series with the power supply to protect the circuit against spark events.

The corona voltage is measured through a voltage divider connected in parallel with the thruster. The total resistance is $R_{tot} = 154 \pm 0.5\,M\Omega$ providing a voltage attenuation ratio of 1:10 000. The corona current is measured using a contactless current probe, featuring a measurement range from 0 A to 0.5 A and an uncertainty of 1%. An analog DC ammeter is employed to determine the ignition voltage due to its high sensitivity in the low current range.
All analog output signals are transmitted to a data acquisition system for processing and analysis.

3.2. Test rig

A dedicated test rig, illustrated in detail in figure 2, is designed to accommodate the thruster inside the low pressure chamber. Most components are 3D printed using ASA polymer with a full filling factor to minimize outgassing during operation, while others are fabricated from PVC.

The emitter frame has a frontal area of $A_e = 150 \times 250\,mm^2$ and houses a constantan wire of $\phi_e = 0.1\,mm$ diameter, which acts as emitter. The wire is wound around an array of pegs that define the emitter spacing s_e, with available configurations given by $s_e = 2.5i\,mm$ with i natural number. The emitter mesh density is defined as $\rho_e = \phi_e/s_e$. HV connection is placed at one corner of the base frame. The collector frame mirrors the geometry of the emitter frame, forming a grid-like structure that is electrically grounded. It features a frontal area of $A_c = 200 \times 250\,mm^2$, with the extended span intended to mitigate electric edge effects. Pegs arrays determine collector spacing of $s_c = 2.5i\,mm$ with i a natural number. The corresponding collector mesh density is defined as $\rho_c = \phi_c/s_c$ where ϕ_c is the collector wire diameter, in this study $\phi_c = 0.1\,mm$. Collector wires are installed only along the direction parallel to the emitter frame. An additional protective cover is mounted on top of the collector frame, slightly reducing the active span of the parallel collector wires to reduce edge effects. The thruster dimensions result from a design trade-off: they must be large enough to generate measurable thrust, particularly under low-pressure conditions, where maximizing the signal-to-noise ratio is critical, yet remain constrained by chamber size. Sufficient clearance is required to prevent the chamber walls from unintentionally acting as grounded collectors.

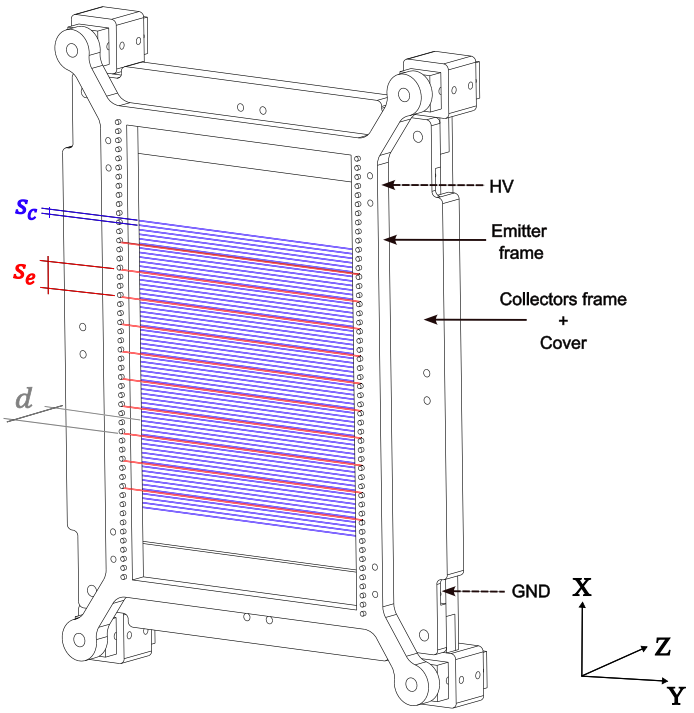

(a) Detail of EAD thruster. Solid arrows indicate the structural frames, while dashed arrows show the locations of the electrical connections. Emitter wires are highlighted in red and the collector grid, positioned parallel to the emitters, is shown in blue. Wires diameter not to scale.

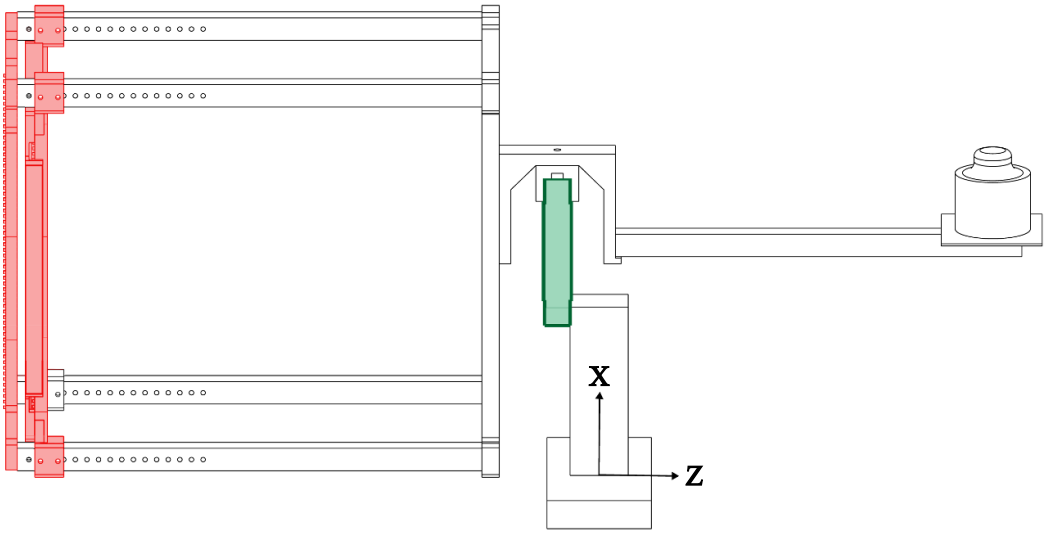

(b) Complete test rig: EAD thruster is highlighted in red while load cell is depicted in green.

Figure 2. Experimental rig.

Both emitter and collector frames are mounted to structural support bars. The emitter frame is fixed, while the collector frame could slide along perforated rails, allowing adjustment of the inter-electrode gap according to $d = (10 + 5i)$ mm with i natural number. A stiffening frame is installed at the opposite end of the support bars to enhance structural rigidity and interface with the load cell system. Its diagonal trusses are designed to avoid flexion and are connected to a U-shaped bracket. The load cell is vertically mounted and connected to its upper side to this bracket via a single-point attachment, while its

base is secured to an iron support platform. All metallic components are grounded. The structure also provides shielding for the load cell from ionic wind effects that could compromise measurements. As the cantilevered weight of the test rig exceeds the rated capacity of the load cell, a counterbalancing arm is installed to neutralize the resulting moment and prevent overload.

3.3. Data acquisition and processing

Three physical quantities are measured during each test: thrust T, corona voltage V_c and corona current i_c. Analog output signals are acquired using a DAQ system connected to a Python script that processes data. Each measurement is obtained by computing the difference in the recorded signal when the thruster is switched on and off. To improve accuracy, multiple acquisitions are performed and averaged to determine the final mean values. Measurement uncertainty is estimated and propagated using the root sum of squares method. Data are sampled at a frequency of $f_s = 25\,\text{kHz}$ over a total acquisition time of $T_{obs} = 2\,\text{s}$.

4. Design of experiment

This section outlines all the geometrical characteristics of the thruster used in the study. The primary objective is to evaluate the influence of pressure p and electrode gap distance d on the EAD performances. All other geometrical parameters are kept constant throughout the test campaign. The adopted configuration is based on [27] and features a parallel wire-to-grid arrangement, without collector wires installed perpendicular to the emitter direction. A detailed summary of the electrode parameters is provided in table 3.

The tested pressures values span from 101 kPa to 20 kPa with decrements of 10 or 5 kPa. The lower pressure limit corresponds to the condition at which further reductions cause the chamber walls to act as dominant collectors when gap was set at 60 mm. The electrode distance was varied from 20 mm to 40 mm in 5 mm increments for thrust and current measurements, with the upper bound also constrained by proximity effects related to the chamber walls, as previously described.

The acquisition of ignition and breakdown voltages followed a separate procedure, given their expected nonlinear dependence on both pressure and gap distance. For this reason, additional data points were collected by extending the gap range up to $d = 60\,\text{mm}$.

5. Results

This section analyses and discusses the results of the experimental campaign. The first step is to evaluate the electrical operational envelope of the thruster, namely the region of stable corona discharge, as this determines where the performance coefficients could be evaluated.

5.1. Ignition voltage: V_{ign}

Ignition voltage is defined as the voltage threshold required for the discharge to develop. The threshold in this experimental campaign is defined as the voltage at which the high sensitivity ammeter starts detecting a current, $i_{ign} = 2.5\,\mu\text{A}$, which is the resolution of the instrument. Multiple acquisitions are performed over a gap range of $20 - 60\,\text{mm}$ and a pressure range of $20 - 101\,\text{kPa}$. Data are displayed in figure 3.

Experimental data are interpolated with a model function that resembles Peek's law [45]:

$$V_{ign}(p,d) = a_1 \cdot p\left(1 + \frac{a_2}{\sqrt{p}}\right)(a_3 + \ln(d)). \tag{13}$$

The suggested fit has an RMSE of 222.4 V, which is an error less than 5% of the local average value.

Ignition voltage is a monotone function of pressure and gap. Ionization occurs when particle collisions are sufficiently energetic to strip electrons from neutral molecules. A decrease in pressure leads to an increase in the mean free path: since the energy of a charged particle is proportional to the electric field, this allows electrons to gain more energy between collisions, hence reducing the amount of input energy and the voltage required to ionize. As for the gap, assuming a reference electric field $E_{ref} = V_c/d$ required for the ionization to occur, a decrease in the electrode gap requires a lower voltage to reach the ionization threshold, so that p and d act on V_{ign} in a similar way.

5.2. Breakdown voltage: V_{br}

The definition of breakdown voltage is not universal, as it depends on the context and application. In this work, the breakdown is defined as the voltage level at which the discharge deviates from corona

Table 3. Adopted thruster configuration for the experimental campaign.

Frame	Type	Diameter (mm)	Spacing (mm)	Mesh density
Emitter	Wire	0.1	17.5	0.0057
Collector	Grid	0.1	2.5	0.04

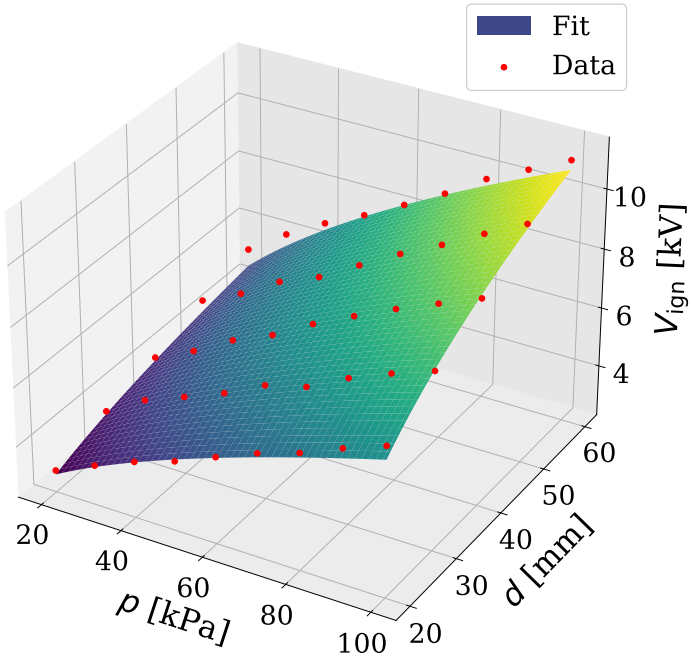

Figure 3. Ignition voltage as a function of p and d.

regime. The transition to another regime, for example glow, streamer or arc depends on pressure as well on electric circuit characteristics [43]. For each pressure and gap, a voltage sweep test is performed acquiring both V_c and i_c. These acquisitions also confirm the quadratic relationship between current and voltage. Breakdown voltage is defined as the peak reached during sweep, as transition leads to a voltage drop accompanied by a sharp increase of current. Due to maximum voltage limitation of the PSU, it was not possible to reach breakdown at high pressure level and large gap.

The breakdown voltage is represented here as a Paschen curve, namely exploiting its dependence on the product pd as shown in (14) and figure 4.

$$V_{\mathrm{br}} = \frac{B \cdot pd}{\ln\left(A \cdot pd\right) - \ln\left[\ln\left(1 + \frac{1}{\gamma}\right)\right]} \tag{14}$$

where A, B are constants depending on the gas used, γ is the secondary electron emission coefficient.

Results show that configurations with the same pd product do not have the same breakdown voltage, this is expected since the original Paschen law applied for a plate-to-plate geometry, while in this case the geometry is not symmetric due to wire-grid arrangements. Moreover, due to high dimensional effects, the curves associated with different gaps do not collapse. This is also confirmed by other studies [46]. In the selected test range, all V_{br} belong to the right branch of the curve, meaning that the Stoletov point was not reached, however data associated to the same gap are interpolated using a Paschen-like curve to estimate its position and then averaged to obtain a global curve. This approximation is used to define the limit of validity of the model presented in section 2 as to the left of the minimum considerations carried out in this work do not hold. The extrapolated value for the Stoletov point $\chi = (pd)_{\mathrm{Stoletov}}$ is in the order of $253.15\,\mathrm{Pa}\cdot\mathrm{m}$ with a weak dependence on d to due the asymmetric geometry of the thruster.The choice of employing this condition as the extra scaling variable for the updated reference geometry is motivated by the fact that the Stoletov point represents a natural scale for ionization phenomena in gas discharges, as it corresponds to the minimum of the Paschen curve and thus identifies the regime of maximum ionization efficiency. Although in this work it has not been possible to directly access this regime experimentally, the value of χ is well defined theoretically and depends primarily on

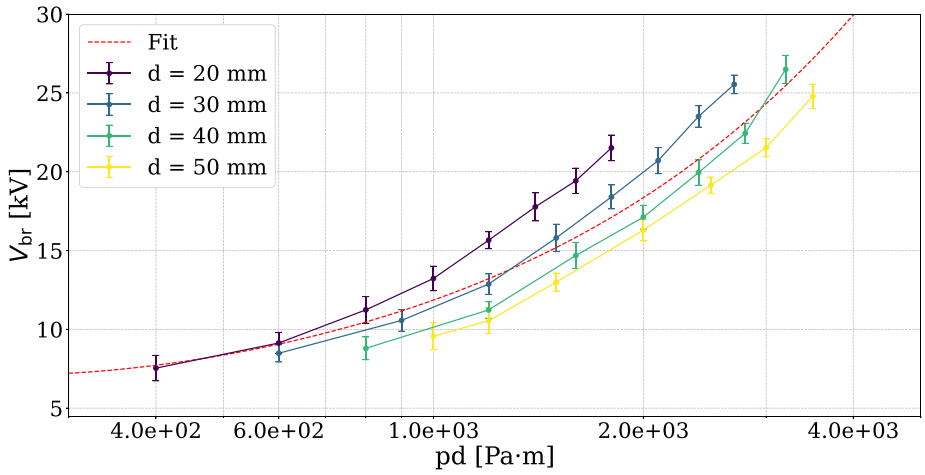

Figure 4. Paschen curve.

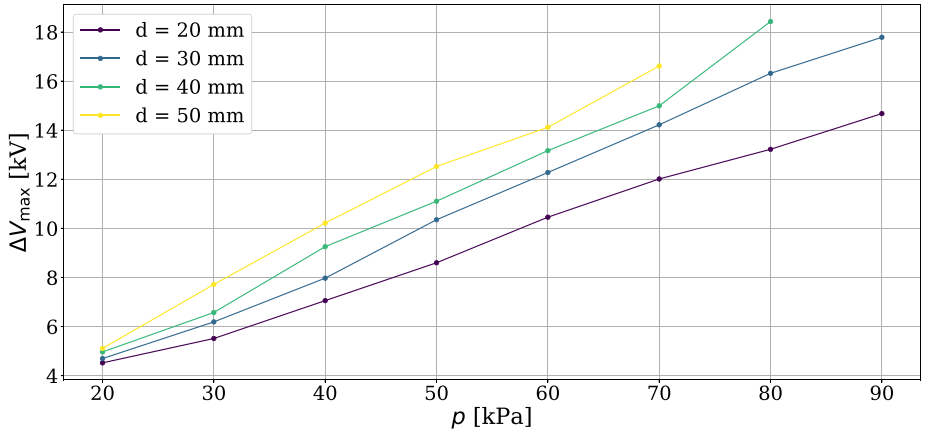

Figure 5. Thruster electrical envelope.

the type of gas, while the geometry of the discharge has only a higher-order effect. Consequently, its use as a normalization parameter is justified: it provides a scale with clear physical meaning without introducing substantial variations in the order of magnitude of the dimensionless results.

The electrical operational envelope of the thruster, shown in figure 5, is defined as:

$$\Delta V_{\max}(p,d) = V_{\mathrm{br}}(p,d) - V_{\mathrm{ign}}(p,d). \tag{15}$$

The voltage envelope increases consistently with both pressure and gap size. This trend is particularly significant at low pressure levels, where the operational voltage range can be quite narrow. By increasing the gap, a broader operational window is achieved, which is advantageous since the required supply voltage remains relatively low at low pressures. A detailed view of $V_{\mathrm{ign}}, V_{\mathrm{br}}$ and available ΔV at fixed gap $d = 20\,\mathrm{mm}$ and pressure $p = 20\,\mathrm{kPa}$ is shown in figure 6 and figure 7 respectively. Data are interpolated using (13) and (14). These experimental data are used in section 5.3.3 to estimate the maximum achievable performance of the thruster, namely exploiting the entire electrical envelope.

5.3. Thruster performance

Thruster performance tests are carried out under variable pressure p and gap d according to what is discussed in section 4. The objective is to evaluate how thrust density T/A and thrust-to-power T/P are affected by the selected variables; moreover, these tests are used to validate the performance dependencies discussed in section 2. Before dealing with the results of the experimental campaign, a discussion about the selected voltage level for all tests is presented. According to the coefficients displayed in table 2, performance depends on both ΔV and V_{c} where $V_{\mathrm{c}} = \Delta V + V_{\mathrm{ign}}$. To compare results without

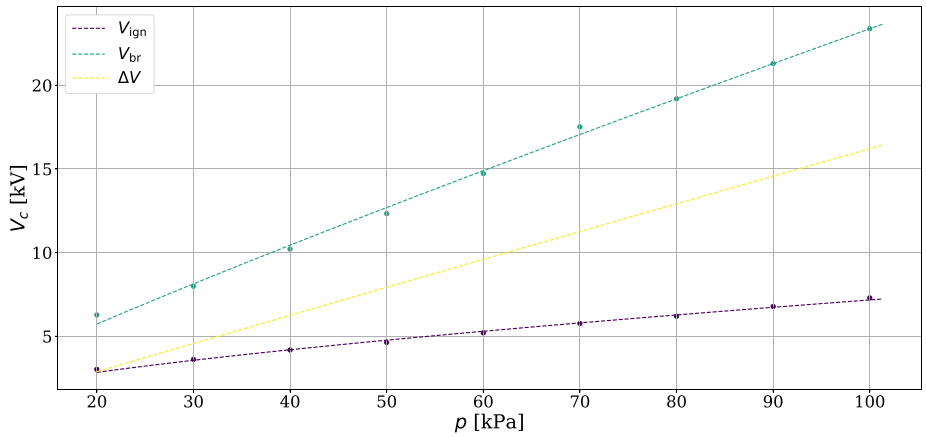

Figure 6. V_{ign}, V_{br} and ΔV vs pressure at $d = 20$ mm.

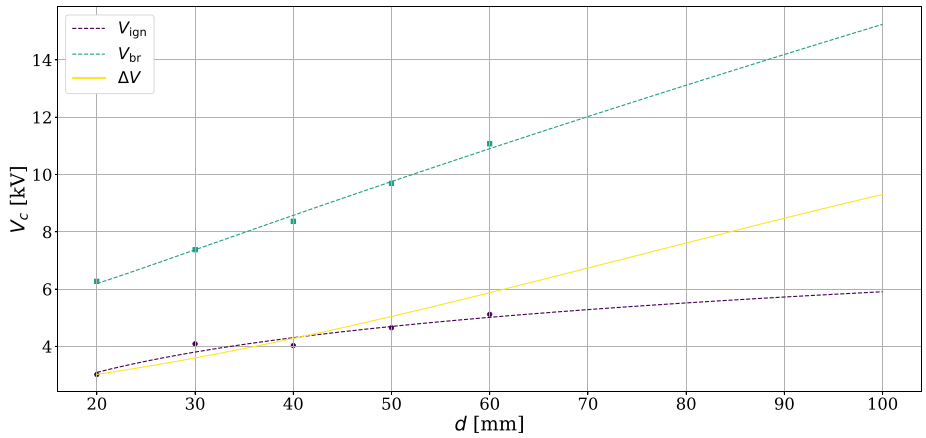

Figure 7. V_{ign}, V_{br} and ΔV vs gap at $p = 20$ kPa.

Table 4. Performance parameters dependencies at fixed ΔV.

Parameter	Proportionality to (p,d)
T/A	p/d
T/P	p^2d^2
i_c	$1/(d^3p)$

Table 5. Reference configuration data.

d	p	V_c	T/A	T/P
20 mm	101 kPa	20 kV	5.4 N m^{-2}	6.39 N kW^{-1}

introducing additional dependencies, all tests are performed at fixed ΔV, the selected voltage value should be sufficiently higher with respect to the ignition voltage to have a reasonable accuracy on the results but sufficiently lower than breakdown voltage to have a safety margin, as electric arcs may be destructive for the electrodes, thus invalidating results. This hypothesis, applied to the performance parameters, leads to the dependencies listed in table 4 where voltage V_c is prescribed:

Experimental data are presented as percentage variations relative to a reference configuration, labeled as *Ref* in the following figures, whose values are provided in table 5.

5.3.1. Performance vs pressure

At first, the performance parameters of an EAD thruster as a function of pressure are evaluated, while the inter-electrode gap is kept fixed at $d = 20$ mm. All results are reported with their mean values and

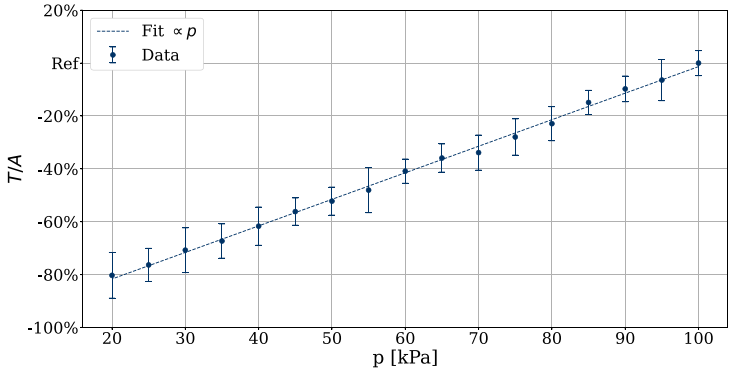

(a) T/A vs p

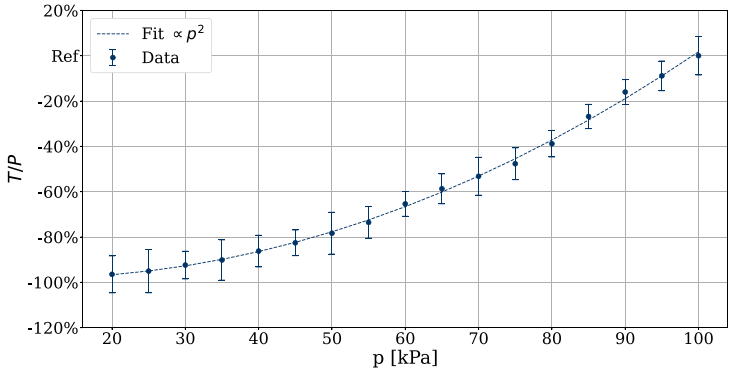

(b) T/P vs p

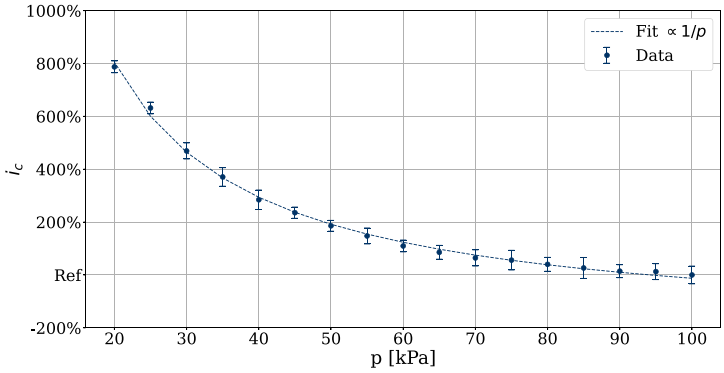

(c) i_c vs p

Figure 8. Thruster performance against pressure p.

with 1σ uncertainty level in figure 8. Data are displayed as a percentage variation with respect to atmospheric pressure level.

Performance figures are strongly affected by pressure, as expected. Thrust density exhibits a linear variation with pressure, this is due to the combined effect of space charge density and local electric field value, which is here attributed exclusively to the charge density due to the model's simplifications. As pressure approaches zero, the thrust produced under corona discharge regime diminishes. This is due to the dependence of collision frequency ν on the gas density ρ; as the gas becomes rarefied, the likelihood of ionizing collisions decreases, even though more ions may be available due to the lower ignition voltage. Ultimately, thrust goes to zero as the number of available neutral molecules also approaches zero. Corona current i_c increases as pressure is lowered, mainly due to the dependence of ion mobility on pressure. Specifically, the lower collision frequency between ions and neutral air molecules at low pressure results in a higher average ion velocity, some ions may even drift between electrodes without colliding. This explains the higher corona current observed at lower pressures. The corona current, as

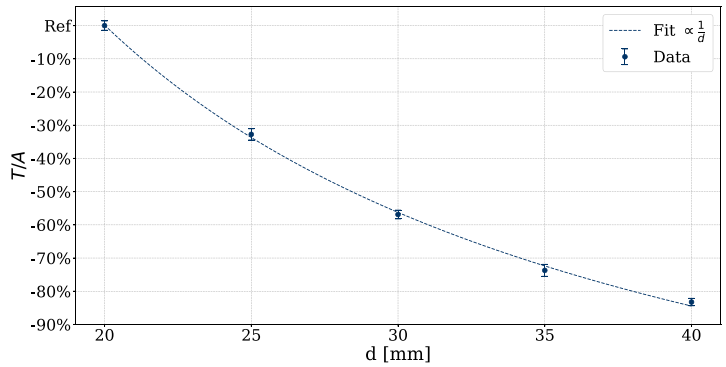

(a) T/A vs d.

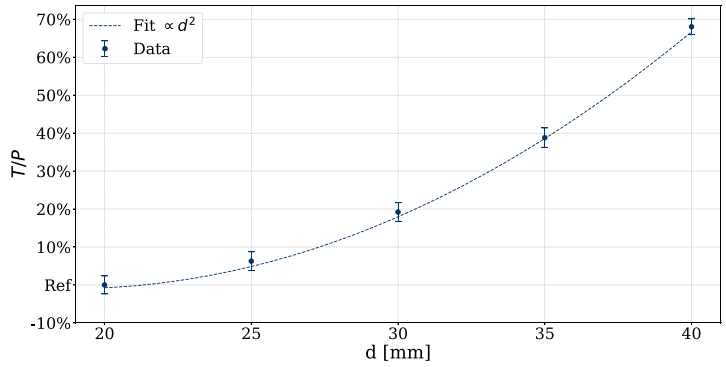

(b) T/P vs d.

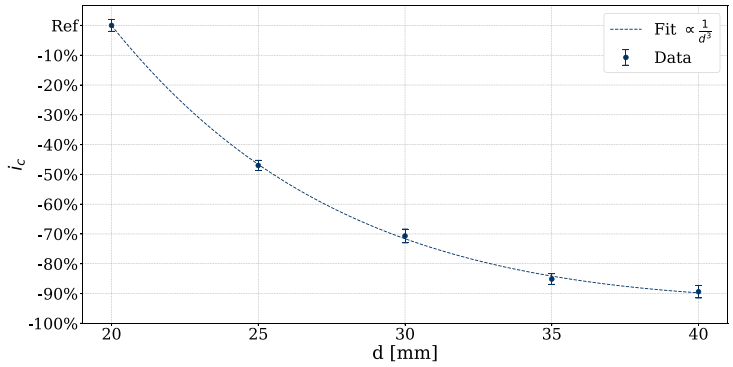

(c) i_c vs d.

Figure 9. Thruster performances against gap d.

well as the corona power P_c, drained by the thruster decreases as $1/p$. The combined effect of generated thrust and power consumption explains the behavior of thrust-to-power ratio T/P, which eventually reaches zero as $p \to 0$.

Experimental data are interpolated with a fit function proportional to pressure according to the dependencies of table 4. Interpolating functions confirm that the predictions of the theoretical model are correct, hence validating the newly defined performance coefficients made in section 2.

5.3.2. Performance vs gap

Experimental EAD thruster performance indices as a function of gap are shown in figure 9, pressure is kept fixed at $p = 101\,\text{kPa}$. All results are reported with their mean values and with 1σ uncertainty level. Data are displayed as a percentage variation with respect to $d = 20\,\text{mm}$.

Thrust density decreases as electrode gap is increased, this is due to an overall reduction of space charge density and average electric field as $d \to \infty$ when ΔV is fixed. Less energy is imparted to charged particles making collision less energetic. The weakening of the electric field also explains the rapid

decrease of corona current i_c. The two combined effects determine the variation of T/P as $d \to \infty$. Less power is required to obtain the same thrust level, hence an higher T/P as gap is enlarged. Experimental data are interpolated with a fit function proportional to the electrode gap according to the dependencies of table 4. Interpolating functions confirm that the predictions of the theoretical model are correct, hence validating the newly defined performance coefficients made in section 2.

5.3.3. Maximum achievable performance

Environmental conditions, represented by pressure, and geometrical parameters, particularly electrode gap, significantly influence T/A and T/P. While the former is determined by the operational environment of the EAD thruster, the latter can be used as a tuning parameter to optimize performances. At fixed pressure, as electrode gap is increased, the electrical envelope of the thruster expands. Thrust density decreases with a dependency of $1/d$, while T/P follows a d^2 trend. Considering an intermediate voltage value between V_{ign} and V_{br}, the choice of electrode gap represents a trade-off between compactness and efficiency, as discussed in multiple literature studies. However, an interesting result arises when the applied voltage is ideally set equal to the breakdown voltage, in order to exploit the total electrical envelope and obtain the maximum thrust. By substituting (13) and (14) into (9) and (12), the proportionality for the maximum achievable thrust density and thrust-to-power can be derived, as shown in (16). The ΔV considered in this model closely follows the maximum voltage envelope retrieved experimentally in figure 5.

$$\left(\frac{T}{A}\right)_{\max} \propto \frac{p\Delta V V_a}{d} \propto \left(\frac{pd}{\ln(pd)} - a_1 \cdot p\left(1 + \frac{a_2}{\sqrt{p}}\right)(a_3 + \ln(d))\right)\frac{pd}{\ln(pd)}\frac{p}{d} \tag{16a}$$

$$\left(\frac{T}{P}\right)_{\max} \propto \frac{p^2 d^2}{V_c} \propto \frac{p^2 d^2}{\frac{pd}{\ln(pd)}}. \tag{16b}$$

Their asymptotic behaviour as $d \to \infty$ is obtained under the verified hypothesis that a_1, a_2, a_3 are small compared to the order of magnitude of d and p:

$$\lim_{d\to\infty}\left(\frac{T}{A}\right)_{\max} \propto d \tag{17a}$$

$$\lim_{d\to\infty}\left(\frac{T}{P}\right)_{\max} \propto d. \tag{17b}$$

These promising results demonstrate that, if a sufficiently powerful PSU is available, both thrust density T/A and thrust to power T/P increase as electrode gap is increased. A similar reasoning can be applied to the asymptotic behavior with respect to pressure. Under the same assumptions, as $p \to \infty$ maximum performances scale according to (16):

$$\lim_{p\to\infty}\left(\frac{T}{A}\right)_{\max} \propto p^3 \tag{18a}$$

$$\lim_{p\to\infty}\left(\frac{T}{P}\right)_{\max} \propto p. \tag{18b}$$

The asymptotic behavior of thruster performances are verified by substituting experimental data from figures 6 and 7 into (16). The corresponding results are presented in figures 10 and 11. In these plots, vertical units are omitted, as only the qualitative shape of the curves is relevant to illustrate the asymptotic trends. Comparison with theoretical predictions indicates that, within the tested pressure range, the thruster already operates in the asymptotic regime corresponding to $p \to \infty$ in the tested pressure range. In contrast, the tested gap values do not yet reach the regime asymptotically equivalent to $d \to \infty$, as a dependence on $\ln(d)$ is still visible. Therefore, the data are extrapolated to larger electrode gaps to evaluate the theoretical trends under that condition.

5.4. EAD performance vs altitude

In previous sections, performances are presented according to their dependence on pressure. In this experimental campaign, temperature Θ is held constant, so that air density depends solely on pressure, $\rho = \rho(p)$. Pressure values are then converted to altitude using the International Standard Atmosphere model. The concept of density altitude h_ρ is introduced as the altitude relative to standard atmospheric conditions at which the air density would be equal to the indicated air density at the place of observation [47]. Since density altitude is a function of temperature, the corresponding variation in

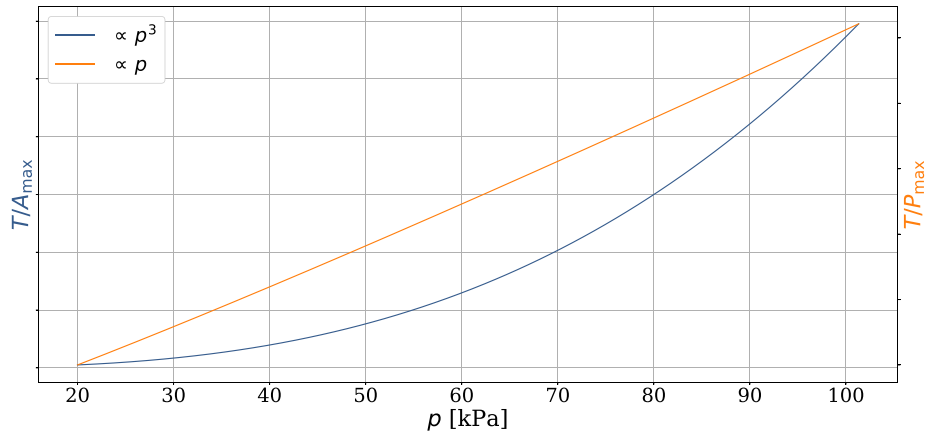

Figure 10. Asymptotic behavior of T/A_{max} and T/P_{max} against pressure.

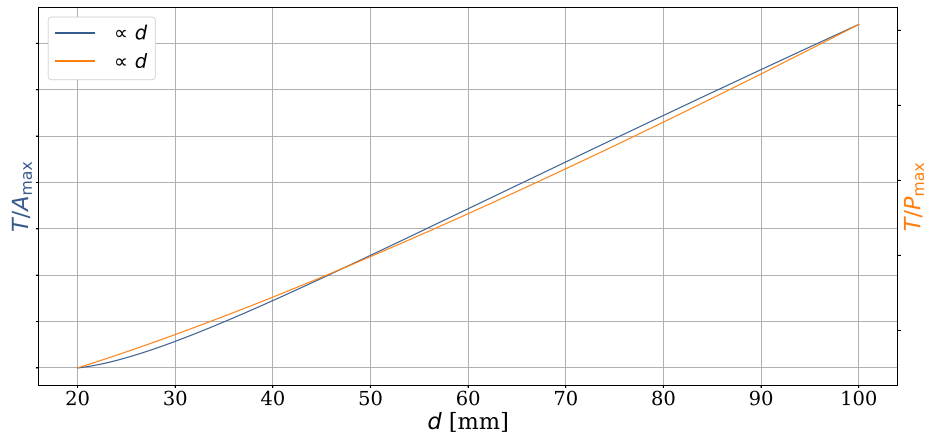

Figure 11. Asymptotic behavior of T/A_{max} and T/P_{max} against gap.

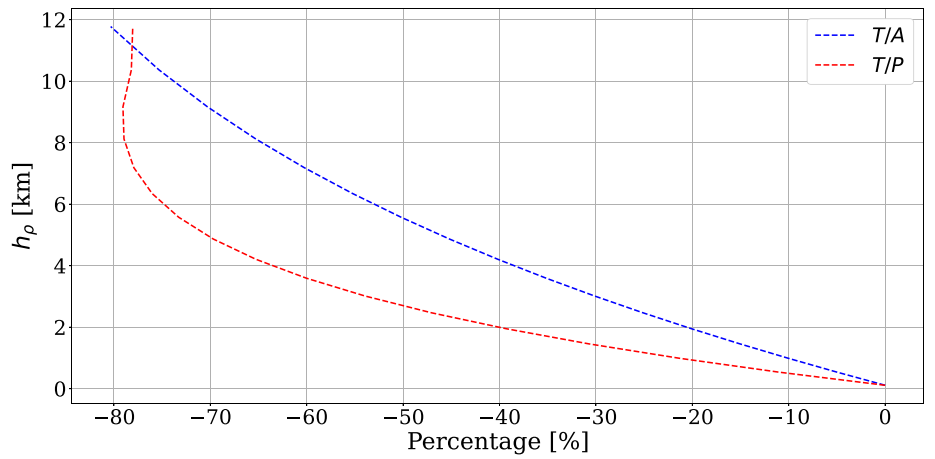

Figure 12. Percentage variation of performance figures vs density altitude h_ρ.

ion mobility is also taken into account. Percentage variation of T/A and T/P as a function of density altitude is shown in figure 12 for a fixed electrode gap $d = 20$ mm and a given ΔV. The thrust density exhibits a monotonic trend, whereas the thrust-to-power ratio displays a minimum, reflecting the different rates at which pressure and temperature change with altitude. This graph can be used to define the ceiling altitude for thruster operation, taking into account the platform on which it is installed.

6. Conclusion

This work presented a study of the performance of EAD thrusters under varying atmospheric pressure p and electrode gap d. Atmospheric conditions are critical in assessing the feasibility of thruster operation in a given environment, while geometric parameters serve as tunable design variables to be optimized based on the chosen thruster layout. An initial theoretical analysis revises and extends previous literature, introducing appropriate scaling laws for key performance metrics. Under simplifying assumptions, dimensionless coefficients for thrust density (T/A) and thrust-to-power ratio (T/P) are derived, enabling meaningful comparisons across different configurations. The theoretical model is validated through an experimental campaign conducted in a low pressure chamber, where pressure was actively controlled and other environmental variables, such as temperature, were monitored. Thrust was measured using a load cell, while corona voltage V_c and corona current i_c were acquired using a voltage divider and a contactless current probe, respectively. The primary focus was on thrust density and thrust-to-power ratio, alongside the ignition voltage V_{ign} and breakdown voltage V_{br}, which define the operational envelope of the thruster. Results show that reducing pressure, effectively simulating higher altitudes, negatively impacts performance, with both T/A and T/P decreasing. Asymptotic analysis further reveals that, when the thruster operates at voltages near breakdown conditions, both T/A and T/P exhibit monotonic growth with increasing gap. Both V_{ign} and V_{br} increase with pressure and gap, consistent with the test regime being on the right-hand side of the Paschen curve. Due to their different dependencies on pressure and gap, the electrical operating envelope expands as both parameters increase. These findings confirm the predictive capability of the theoretical model. The model is intended to be applied only under corona discharge regime. No significant deviations are expected until the pd product approaches the minimum of the Paschen curve, namely Stoletov point, beyond which alternative scaling behaviors may emerge. Finally, maximum achievable performance, under electrical limitations, are predicted using obtained scaling laws and verified using experimental data. Future developments should include testing under varying environmental temperature and humidity levels to fully characterize EAD thruster behavior in realistic operating conditions, extending beyond the controlled environment of laboratory experiments.

Data availability statement

The data that support the findings of this study are openly available at the following URL/DOI: https://doi.org/10.5281/zenodo.17085847.

Acknowledgments

This project has received funding from the European Union's Horizon Europe Research and Innovation Programme under Grant Agreement No 101098900. Views and opinions expressed are however those of the authors only and do not necessarily reflect those of the European Union or European Innovation Council and SMEs Executive Agency (EISMEA). Neither the European Union nor the granting authority can be held responsible from them.

ORCID iDs

D Usuelli 0000-0003-2910-9053
A Favalli 0009-0009-9895-194X
S Trovato 0000-0002-1479-4572
R Terenzi 0000-0002-3126-1786
M Belan 0000-0001-7040-0286

References

[1] Cao W, Mecrow B C, Atkinson G J, Bennett J W and Atkinson D J 2012 *IEEE Trans. Ind. Electron.* **59** 3523–31
[2] Brelje B J and Martins J R 2019 Electric, hybrid and turboelectric fixed-wing aircraft: a review of concepts, models and design approaches *Prog. Aerosp. Sci.* **104** 1–19
[3] Brand J, Sampath S, Shum F, Bayt R and Cohen J Potential use of hydrogen in air propulsion
[4] Goebel D M and Katz I 2008 *Fundamentals of Electric Propulsion: Ion and Hall Thrusters* (Wiley)
[5] Mazouffre S 2016 Electric propulsion for satellites and spacecraft: established technologies and novel approaches *Plasma Sources Sci. Technol.* **25** 033002
[6] Charles C 2009 *Plasmas Spacecr. Propulsion* **42** 163001

[7] Xu H, He Y, Strobel K, Gilmore C, Kelley S, Hennick C, Sebastian T, Woolston M, Perreault D and Barrett S 2018 Flight of an aeroplane with solid-state propulsion *Nature* **563** 532–5
[8] Khomich V and Rebrov I 2018 In-atmosphere electrohydrodynamic propulsion aircraft with wireless supply onboard *J. Electrost.* **95** 1–12
[9] Townsend J 1914 XI. The potentials required to maintain currents between coaxial cylinders *London, Edinburgh Dublin Phil. Mag. J. Sci.* **28** 83–90
[10] Fridman A and Kennedy L 2004 *Plasma Physics and Engineering* (Taylor & Francis)
[11] Wilson J, Perkins H and Thompson W 2009 An investigation of ionic wind propulsion *Technical Report* NASA/TM-2009-215822 NASA
[12] Belan M, Baldo J, Kahol O and Montenero D 2024 Blade emitters for atmospheric ionic thrusters *J. Phys. D* **57** 195201
[13] Kaci M, Said H A, Laifaoui A, Aissou M, Nouri H and Zebboudj Y 2015 Investigation on the corona discharge in blade-to-plane electrode configuration *Braz. J. Phys.* **45** 643–55
[14] Ieta A and Chirita M 2019 Electrohydrodynamic propeller for in-atmosphere propulsion; rotational device first flight *J. Electrost.* **100** 103352
[15] Drew D and Follmer S 2021 High force density multi-stage electrohydrodynamic jets using folded laser microfabricated electrodes *21st Int. Conf. on Solid-State Sensors, Actuators and Microsystems (Transducers)* (Institute of Electrical and Electronics Engineers), pp 54–57
[16] Chirita M and Ieta A 2022 First rotary ionic engine with contra-rotating propellers *J. Propuls. Power* **38** 893–900
[17] Belan M, Terenzi R, Trovato S and Usuelli D 2022 Effects of the emitters density on the performance of an atmospheric ionic thruster *J. Electrost.* **120** 103767
[18] Moreau E, Benard N, Lan-Sun-Luk J D and Chabriat J P 2013 Electrohydrodynamic force produced by a wire-to-cylinder dc corona discharge in air at atmospheric pressure *J. Phys. D* **46** 475204
[19] Ieta A, Ellis R, Citro D, Chirita M and D'Antonio J 2013 Characterization of corona wind in a modular electrode configuration *Proc. ESA Annual Meeting on Electrostatics* (*Cocoa Beach ,FL*) pp 1–7
[20] Belan M, Arosti L, Polatti R, Maggi F, Fiorini S and Sottovia F 2021 A parametric study of electrodes geometries for atmospheric electrohydrodynamic propulsion *J. Electrost.* **113** 103616
[21] Xu H, Gomez-Vega N, Agrawal D and Barrett S 2019 Higher thrust-to-power with large electrode gap spacing electroaerodynamic devices for aircraft propulsion *Appl. Phys. Lett.* **53** 025202
[22] Gomez-Vega N and Barrett S R H 2024 Order-of-magnitude improvement in electroaerodynamic thrust density with multistaged ducted thrusters *AIAA J.* **62** 1342–53
[23] Kahol O, Belan M, Pacchiani M and Montenero D 2023 Scaling relations for the geometry of wire-to-airfoil atmospheric ionic thrusters *J. Electrost.* **123** 103815
[24] Usuelli D, Terenzi R, Trovato S and Belan M 2024 Performance enhancement of EAD thrusters with nonuniform emitters array *IEEE Trans. Plasma Sci.* **52** 5414–21
[25] Lemetayer J, Marion C, Fabre D and Plouraboué F 2022 Multi-inception patterns of emitter array/collector systems in DC corona discharge *J. Phys. D* **55** 185203
[26] Arif S, Branken D J, Everson R C, Neomagus H W J P and Arif A 2018 The influence of design parameters on the occurrence of shielding in multi-electrode ESPs and its effect on performance *J. Electrostat.* **93** 17–30
[27] Raffaello T, Trovato S, Usuelli D and Belan M 2025 *Nat., Sci. Rep.* **15** 41513
[28] Vega N, Xu H, Abel J and Barrett S 2021 Performance of decoupled electroaerodynamic thrusters *Appl. Phys. Lett.* **118** 074101
[29] Xu H, He Y and Barrett S 2019 A dielectric barrier discharge ion source increases thrust and efficiency of electroaerodynamic propulsion *Appl. Phys. Lett.* **114** 254105
[30] Orriére T, Moreau Eric and Pai D Z 2019 Electric wind generation by nanosecond repetitively pulsed microplasmas *J. Phys. D: Appl. Phys.* **52** 464002
[31] Lacoste D, Pai D and Laux C 2004 *Ion Wind Effects in A Positive DC Corona Discharge in Atmospheric Pressure Air* (American Institute of Aeronautics and Astronautics)
[32] Guerra-Garcia C, Nguyen N, Mouratidis T and Martinez-Sanchez M 2020 Corona discharge in wind for electrically isolated electrodes *J. Geophys. Res. Atmos.* **125** e2020JD032908
[33] Grosse S, Benard N and Moreau E 2024 Electroaerodynamic thrusters: influence of a freestream on the current, ionic wind and force produced by a DC corona discharge *J. Electrost.* **130** 103950
[34] Trovato S, Terenzi R, Usuelli D and Belan M 2024 Wind tunnel testing and performance modeling of an atmospheric ion thruster *J. Phys. D: Appl. Phys.* **58** 015201
[35] Riboldi C, Belan M, Cacciola S, Terenzi R, Trovato S, Usuelli D and Familiari G 2024 Preliminary sizing of high-altitude airships featuring atmospheric ionic thrusters: an initial feasibility assessment *Aerospace* **11** 590
[36] van Wynsberghe E and Turak A 2016 Station-keeping of a high-altitude balloon with electric propulsion and wireless power transmission: a concept study *Acta Astronaut.* **128** 616–27
[37] Gilmore C K and Barrett S R 2018 Electroaerodynamic thruster performance as a function of altitude and flight speed *AIAA J.* **56** 1105–17
[38] Grosse S, Benard N and Moreau E 2025 Current, thrust and power of a corona discharge plasma thruster at tropospheric altitude *J. Phys. D* **58** 095201
[39] Khomich V, Malanichev V and Rebrov I 2021 Electrohydrodynamic thruster for near-space applications *Acta Astronaut.* **180** 141–8
[40] Zhao Y, Chen S, Li K, Wang T and Wang F 2024 Influence of humidity and air pressure on thrust characteristics of ion wind propulsion systems *J. Phys. D: Appl. Phys.* **57** 415201
[41] Vaddi R, Guan Y, Mamishev A and Novosselov I 2020 Analytical model for electrohydrodynamic thrust *Proc. R. Soc. A* **476** 20200220
[42] Gilmore C and Barrett S 2015 Electrohydrodynamic thrust density using positive corona-induced ionic winds for in-atmosphere propulsion *Proc. R. Soc. A* **471** 20140912
[43] Chen F 2016 *Introduction to Plasma Physics and Controlled Fusion* (Springer International Publishing)

[44] Mason E A and McDaniel E W 1988 *Transport Properties of Ions in Gases* vol 89 p 15174
[45] Peek F 1920 *Dielectric Phenomena in High Voltage Engineering* (McGraw-Hill, Inc.)
[46] Bowers W and Gershaft S 2023 Investigation of the paschen curve for various electrode geometries in iec fusion devices through monte carlo simulations (arXiv:2309.07184)
[47] NOAA N and United States Air Force 1976 U.S. standard atmosphere, 1976 (U.S. Government Printing Office) available from NASA Technical Reports Server (NTRS)